Journal of Magnetic Resonance 212 (2011) 102–108

Contents lists available at ScienceDirect

Journal of Magnetic Resonance

journal homepage: www.elsevier.com/locate/jmr

Two-dimensional T_2 distribution mapping in porous solids with phase encode MRI

Oleg V. Petrov *, Bruce J. Balcom

MRI Research Centre, Department of Physics, University of New Brunswick, Fredericton, Canada

ARTICLE INFO

Article history:
Received 2 May 2011
Revised 16 June 2011
Available online 25 June 2011

Keywords:
T_2 mapping
SPRITE
Spin-echo SPI
Compressed sensing
Porous solids

ABSTRACT

Two pure phase encode MRI sequences, CPMG-prepared SPRITE and spin-echo SPI with compressed sensing, for two-dimensional (2-D) T_2 distribution mapping have been presented. The sequences are 2-D extensions of their 1-D predecessors previously described and are intended for studying processes in porous solids and other samples with short relaxation times whenever 2-D T_2 maps are preferable to simple 1-D profiling. The sequences were tested on model samples and natural water-saturated rocks, in a low field MRI instrument. 2-D spin-echo SPI and CPMG-SPRITE demonstrate a similar performance, enabling measurement of T_2 down to 1–2 ms. Both experiments are time consuming (up to 2–2.5 h sample dependent). As such, they can be recommended mostly for measurement during steady state conditions or when studying relatively slow dynamic processes (e.g. enhanced oil recovery, cement paste hydration, curing rubber, infiltration of paramagnetic ions).

1. Introduction

Recently [1], we introduced two pulse sequences for one-dimensional (1-D) T_2 distribution mapping with pure phase encode MRI, namely CPMG-prepared SPRITE and spin-echo SPI. The sequences were intended primarily for experiments on fluids in reservoir rocks, building materials and other porous solids, where using frequency encode MRI is often problematic either due to local gradient distortions or too short T_2. 1-D T_2 mapping is well suited for studying unidirectional processes in axially symmetric samples. There are the cases, however, when two-dimensional (2-D) T_2 mapping may be required, e.g., displacement processes in enhanced oil recovery and examples where the sample and process are not suitably symmetric. To meet such needs, we have extended the previous sequences to 2-D, adhering to pure phase spatial encoding. The sequences were tested on model samples and natural water-saturated rocks, using a low-field MRI instrument, as presented below.

2. CPMG-prepared Spiral SPRITE

2.1. The pulse sequence

CPMG-prepared SPRITE implements the T_2 mapping scheme in which the spatial encoding of the signal follows the T_2 relaxation. The 2-D version of the sequence differs from its previous 1-D version [1] only in using the Spiral SPRITE instead of the double half k-space (DHK) SPRITE pulse sequence for spatial encoding. The pulse sequence diagram is presented in Fig. 1. The magnetization is partly relaxed during a CPMG train and stored along z-axis, then the Spiral SPRITE is applied. To remove the 'unprepared' component from a SPRITE signal, we store the transverse magnetization after the CPMG train alternately upwards and downwards on the z-axis, in two scans, and then subtract one from another [2]. The resulting difference signal is given by

$$M_{xy}(n) = 2M_z(0)\sin\alpha(\cos\alpha e^{-t_r/T_1})^{n-1} \quad (1)$$

where $M_z(0) = M_{eq}e^{-2mTE/T_2}$ is z-magnetization prepared by the CPMG train with m pulses and a pulse period TE; M_{eq} the equilibrium z-magnetization; n an α-pulse number and α the pulse flip angle ($\sim 10°$). The derivation of Eq. (1) is given in the Appendix A. To increase SNR, we acquire four FID points after each α-pulse and then reconstruct the image by the chirp-z transform [3]. The spoiling gradients are applied after the z-storage to destroy the partially recovered longitudinal magnetization brought into the xy-plane by the z-storage pulse.

The Spiral SPRITE pulse sequence employs a k-space trajectory with four interleaves [3]. Each interleaf comprises 158 or 648 k-samples for 32×32 or 64×64 image resolution, respectively, which takes about 0.1–0.3 s at TR = 0.5 ms. This is less than the repetition time between scans when measuring water- or brine-saturated samples ($\sim$2 s). In these, typical, cases the total duration of the experiment will be only slightly longer than in the predecessor 1-D version and will remain proportional to the T_2 dimension, at least for low image resolutions.

The T_2 mapping scheme used in CPMG-prepared SPRITE imposes no particular restrictions on the echo time (TE). As such, it is expected to provide the same range of measurable T_2 as the

* Corresponding author. Fax: +1 506 453 4581.
E-mail address: opetrov@unb.ca (O.V. Petrov).

1090-7807/$ - see front matter © 2011 Elsevier Inc. All rights reserved.
doi:10.1016/j.jmr.2011.06.018

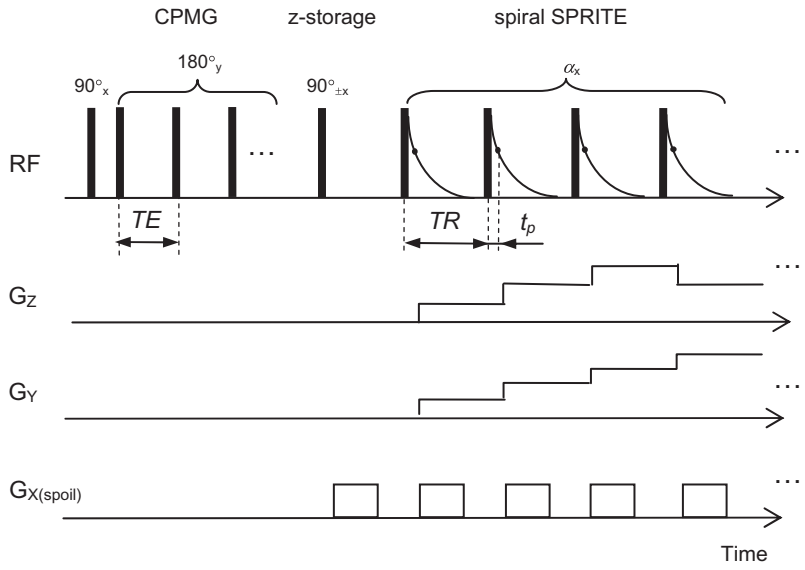

Fig. 1. Spiral SPRITE with CPMG-prepared magnetization and alternating *z*-storage. Time intervals used were: $TE = 0.4$ ms, $TR = 1$ ms, $t_p = 0.1$ ms, and $\alpha = 10°$. In actual experiments, four FID points were acquired after every α -pulse, with a dwell time of 8 μs. The first spoiler-gradient is applied to dephase partially recovered longitudinal magnetization brought into the *xy*-plane by the *z*-storage pulse. Subsequent spoiling gradients are unnecessary but can help yield a smoother (monotonic) SPRITE signal attenuation at the following *k*-space points.

regular CPMG sequence. A drawback is a relatively low sensitivity (SNR) due to the low flip angle of the SPRITE pulses. The evolution of M_z toward a longitudinal steady state during *k*-space sampling, controlled by T_1, will cause image blurring (see below), which may be significant.

2.2. Test measurements

Fig. 2 shows local T_2 decays obtained with CPMG-SPRITE at central and two marginal points of the image of a vial with Gd-doped water ($T_1 = 100$ ms). The decays follow a regular CPMG curve, giving the same T_2 value.

The next test was conducted on two natural rock samples – Berea and Wallace sandstones, saturated with water, to examine the sequence for its ability to reproduce reference T_2 distributions. Due to a low porosity (14% and 22%) and long T_1 (up to 1 s) of the samples, it took almost 3 min to acquire an image of acceptable quality (Fig. 3). We collected 50 T_2 weighted images, with logarithmically spaced T_2 steps, the total acquisition time being 2.5 h. Fig. 3a shows T_2 distributions measured at three different positions across the Berea sample (marked by circles). As compared to regular CPMG measurements (Fig. 3a, dotted line), the T_2 distributions by CPMG-SPRITE miss T_2 components shorter than 1 ms. This is more pictorial for the Wallace sample (Fig. 3b), where the short T_2 components contribute about 25% of the distribution. Some components on the long T_2 side of distributions are missing. Because our primary concern is reproducibility of short T_2 components, we will not discuss the long T_2 part further. To check whether the inability of CPMG-SPRITE to detect T_2 under 1 ms is due to a poor SNR of spatially resolved T_2 decays (and, as a consequence, the inability of an ILT algorithm to reproduce T_2 distributions in all details), we acquired the integral (bulk) signal by running the same experiment but without applying gradients. The resulting T_2 distribution showed no considerable difference compared to the distributions measured from pixels' decays. Thus, the factor of SNR must be excluded. We point out that the 1-D version of the sequence [1] has a better capability to measure short T_2, and the only difference between the sequences is the number of

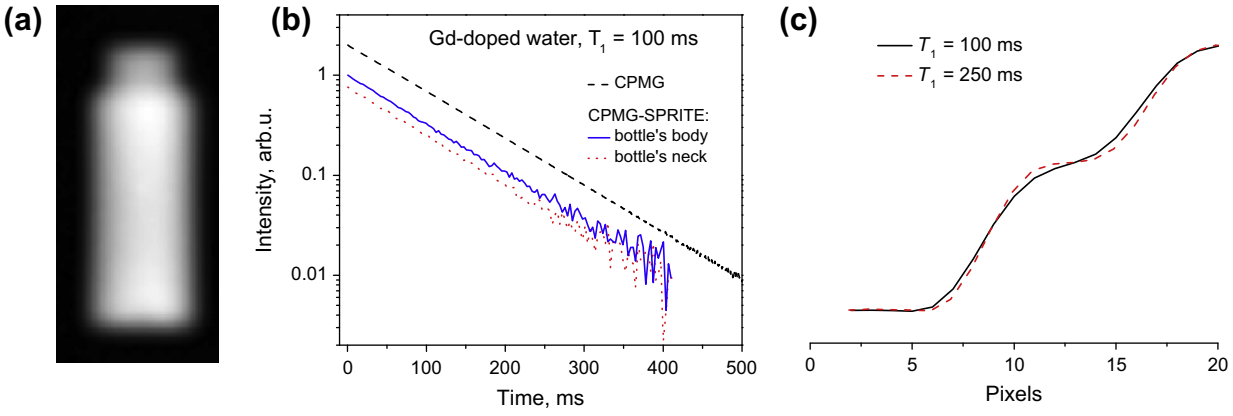

Fig. 2. (a) A 64 × 64 CPMG-SPRITE image of a bottle of Gd-doped water ($T_1 = 100$ ms). (b) T_2-decays measured at two different locations of the bottle. A good agreement between spatially resolved and bulk T_2 measurements is observed. (c) Partial profile along the object, from the top, for two different sample T_1's. The longer T_1 yields a sharper image.

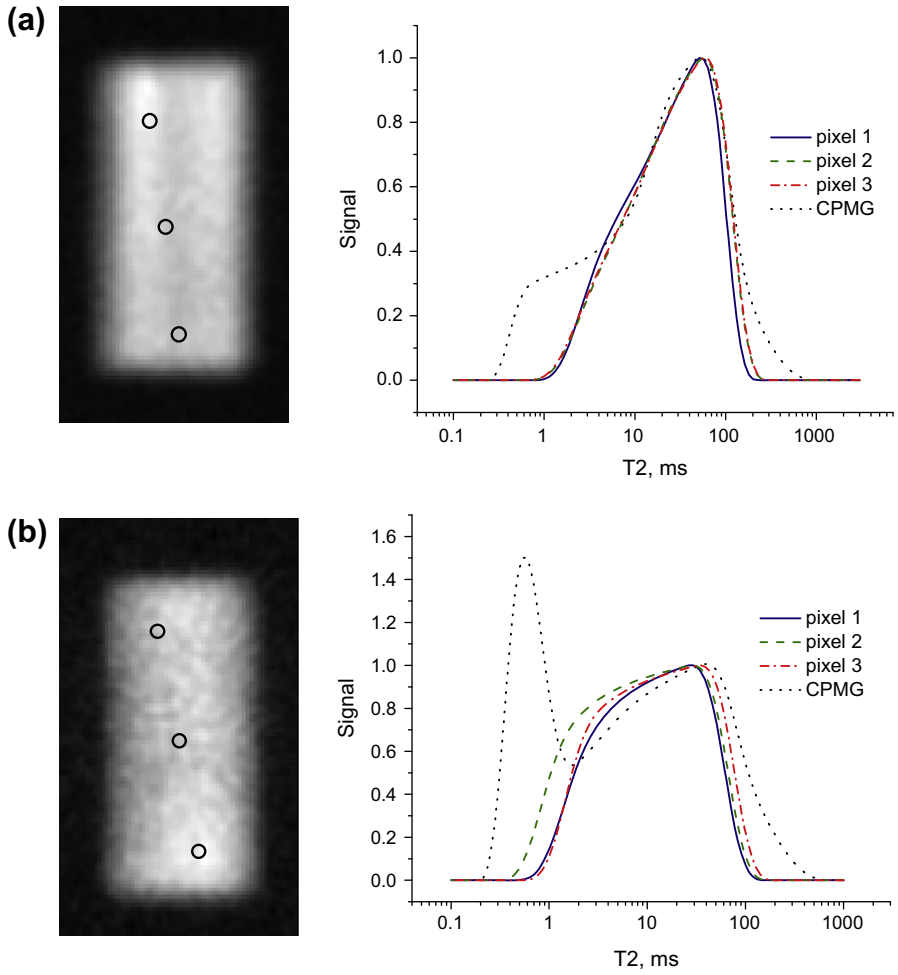

Fig. 3. (a, left) A 64 × 64 CPMG-SPRITE image of Berea sandstone saturated with water. (a, right) T_2 distributions measured at three different pixels across the sample (shown by the circles on the left), in comparison to regular CPMG measurements. (b) As above but for Wallace sandstone.

the SPRITE α-pulses applied during a scan (648 versus 32). We will return to this issue in the concluding Section 4.

The last test was performed on two pieces of Wallace sandstone saturated with water and mineral oil. The first echo image (Fig. 4) shows no T_2 contrast between the fluids, which makes the technique suitable for quantitative analysis. T_2 distributions measured on water- and oil-containing parts miss some components on both sides, but preserve the mean T_2 characteristic for these fluids.

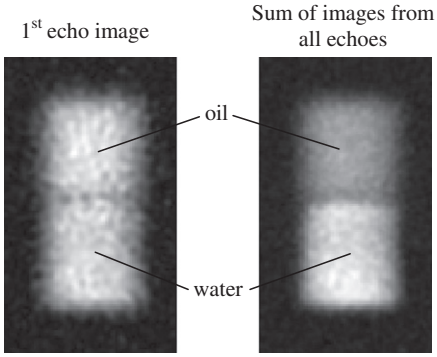

Fig. 4. 64 × 64 CPMG-SPRITE images of two pieces of Wallace sandstone: one saturated with mineral oil and the other with water. *Left:* The 1st echo image, showing equal intensities from oil- and water-saturated halves. *Right:* A sum of images from all echoes with the intensities weighted by the arithmetic mean T_2 of oil and water.

3. Spin-echo SPI with compressed sensing

3.1. The pulse sequence

In SE-SPI (Fig. 5a), the magnetization is first spatially encoded within the first pulse interval τ_0 and then is read out upon multiple refocusing with the period *TE*. To preserve both *x*- and *y*-component of magnetization upon refocusing, an XY-8 phase cycle is applied [4]. From 7 to 14 echo time points are acquired, which are then summed and reconstructed into a single image with a given T_2 weight:

$$M_{xy}(m) = M_{eq} e^{-2\tau_0/\tilde{T}_2} e^{-2(m-1)TE/T_2} \quad (2)$$

where M_{eq} is the equilibrium *z*-magnetization and $\tilde{T}_2$ the relaxation constant for the first pulse interval $2\tau_0$ ($\tilde{T}_2 \geqslant T_2$). The first echo acquisition time is limited to 1.2–1.6 ms due to the presence of encoding gradients between the first two r.f. pulses. This limit is controlled by hardware and can be lowered by using faster rise time gradients and an appropriate correction of the gradient pulses [5].

The measurement time in SE-SPI is proportional to the *k*-space dimension rather than the T_2 dimension. Adhering to the pure phase encoding, we thereby come to the problem of an *N*-fold increase in the number of scans when changing the sequence from

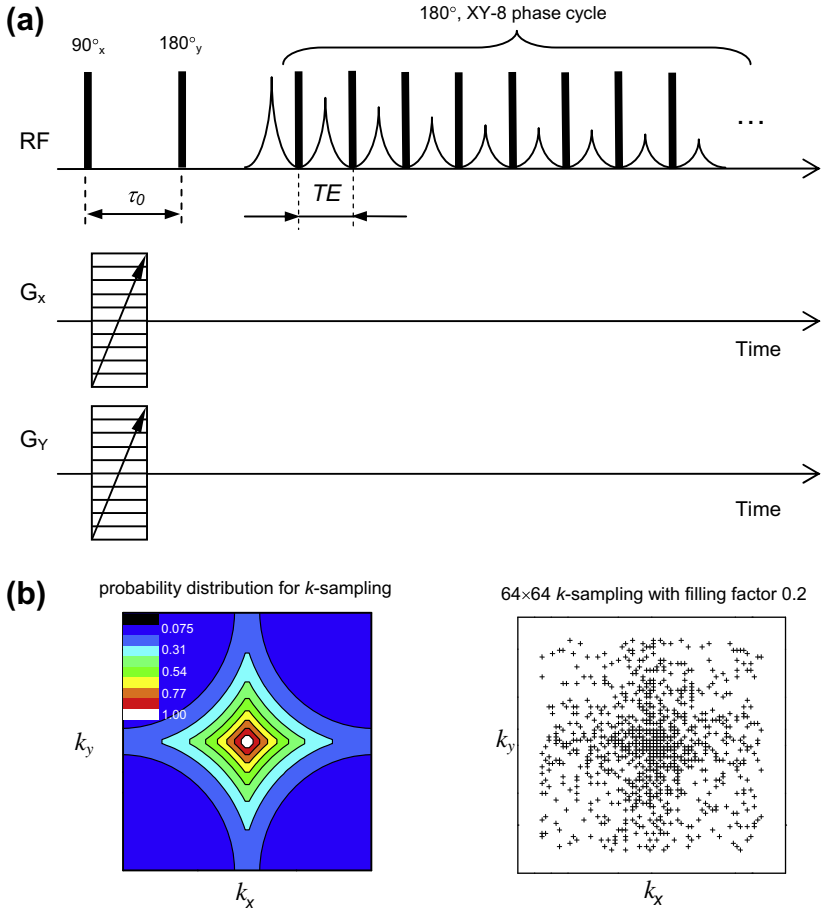

Fig. 5. (a) 2-D spin-echo SPI sequence. The magnetization is phase encoded during the first pulse interval with τ_0 = 0.8 ms and then read out through multiple refocusing with *TE* = 0.4 ms. To preserve the phase shift upon refocusing, an XY-8 phase cycle is applied. Composite pulses were used for r.f. field inhomogeneity compensation [13]; namely, the sequences $45_{\pi/2}90_0 90_{3\pi/2}45_0$ for a composite 90° pulse and $180_{2\pi/3}180_{4\pi/3}180_{2\pi/3}$ for a composite 180° pulse. (b) A *k*-sampling distribution function (left) and a corresponding 64 × 64 mask (right), providing a 5-fold acquisition acceleration.

1-D to 2-D. To solve, at least partly, that problem, we make use of compressed sensing, a technique that permits one to recover an image from a number of *k*-samples smaller than the desired resolution of the image [6]. Namely, instead of acquiring all $N_x \times N_y$ samples with the Nyquist period (where $N_x \times N_y$ is the required image dimension), we choose only 20% guided by the probability distribution function shown in Fig. 5b. The distribution makes a preference for the samples that bear the highest signal intensity, and the central *k*-space point is always included. A similar strategy of *k*-sampling has been used in [9,10]. The image is recovered by using the Split Bregman method for compressed sensing [7]. According to [8], this is the fastest algorithm for image reconstruction via l_1-minimization, which is essential in our case because tens to hundreds of T_2-weighted images are to be reconstructed after every SE-SPI experiment. The reconstruction procedure is outlined in the Appendix B. The typical reconstruction time is 1–2 s per image on a PC laptop with Pentium 4, depending on the image resolution and number of iterations.

3.2. Test measurements

Fig. 6 shows the effect of the sparse *k*-space sampling on the image quality. The phantom was a vial of water doped with $GdCl_3$, and the image resolution was 64 × 32 pixels. The quality visibly deteriorates as the percentage of acquired *k*-points decreases. However, the deterioration is not dramatic, and such details of the image as the air bubble near the vial neck and the Gibbs ringing pattern remain distinguishable down to 5-fold reduction of *k*-samples. What is more significant is that the reduction preserves T_2 decays for all the image pixels (Fig. 7), thus enabling T_2 mapping, which is of far greater importance in our applications than the image quality.

Fig. 8a shows a 64 × 32 image of the water-saturated Berea sample reconstructed from 20% of *k*-values. Given NS = 8 and the repetition delay 2 s, the acquisition took 2 h. T_2 distributions measured across the sample miss the T_2 components shorter than 2 ms in comparison to the CPMG measurement (dashed line). This is a consequence of the limited first echo acquisition time (1.2–1.6 ms), owing to the presence of encoding gradient pulses. The Walace sandstone sample exhibits the same cutoff at T_2 = 2 ms (Fig. 8b).

Fig. 9 shows an SE-SPI image of the composite sample of two pieces of Wallace sandstone saturated with water and mineral oil. Unlike CPMG-SPRITE (see Fig. 4), SE-SPI introduces a disproportion to water and oil intensities in the first echo image, namely the oil-saturated half appears brighter than the water-saturated one.

4. Discussion and conclusion

The sequences presented herein are a further development of T_2 mapping with pure phase-encode MRI. The CPMG-prepared SPRITE is a straightforward extension of the previous 1-D version of the sequence [1], with the only difference being the use of a spiral *k*-space trajectory in place of a linear one. Such a replacement does not entail

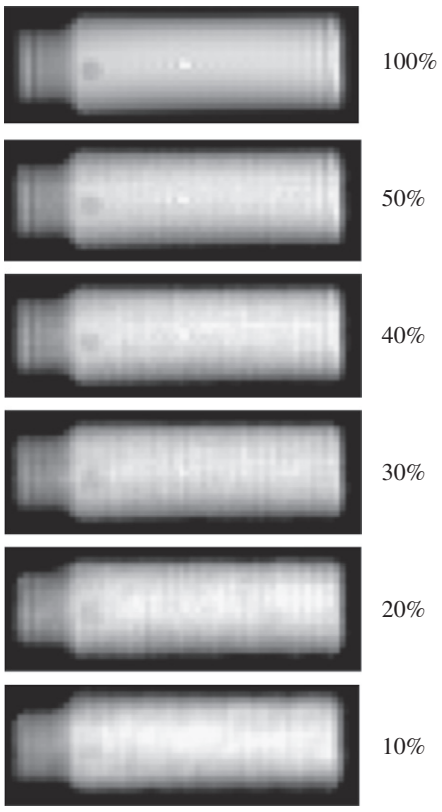

Fig. 6. The effect of sparse sampling on the image quality. The dark spot near the bottle's neck is an air bubble.

a serious elongation of the experiment, though it will require more scans to recover the SNR achievable in 1-D CPMG-SPRITE. To diminish T_1-attenuation of the k-space signal during spiral sampling (see Eq. (1)), hence to reduce blurring, the k-sampling is implemented in four spiral interleaves, thereby further increasing the number of scans. In the measurements on the water-saturated sandstones given in Section 2.2, it took $24 \times 4 = 96$ scans and about 3 min to acquire a single T_2-weighted image. This example, though rather unfavorable in the sense of SNR, stresses the importance of acquiring only the necessary T_2-weighted images for ILT with an optimized sampling (e.g. logarithmic).

Although a regular CPMG sequence is employed for the T_2-preparation, without a particular restriction on TE, the T_2 distributions by CPMG-SPRITE miss components on either side of the T_2 spectrum in comparison to the regular CPMG measurements. It is noteworthy that the 1-D version of the sequence *is* capable of measuring T_2 as short as a regular CPMG sequence [1]. Increasing SNR is found not to extend the limits of measurable T_2's (see Section 2.2). Therefore, one can only consider the lengthy α -pulse train and the resulting T_1-attenuation of the k-signal to be the cause of loosing short T_2 components. Namely, taking into account the correlation between T_1 and T_2, one may expect that the point spread function for short T_2 components will be broader than for long T_2 components, due to the stronger T_1 attenuation. As a result, short T_2 components will have a poorer SNR in the image, which, in turn, may affect relative intensities in the measured T_2 distribution.

In the other sequence, 2-D SE-SPI, the acquisition time is proportional to the number of k-samples rather than the T_2 dimension. This necessitates the use of a sparse (compressive) k-sampling with the number of samples considerably smaller than the desired image resolution. The image reconstruction is implemented, in this case, by l_1-minimization instead of FFT (see the Appendix B). Since the image quality depends on both the k-space sampling mask chosen and the reliability of a reconstruction algorithm, this technique

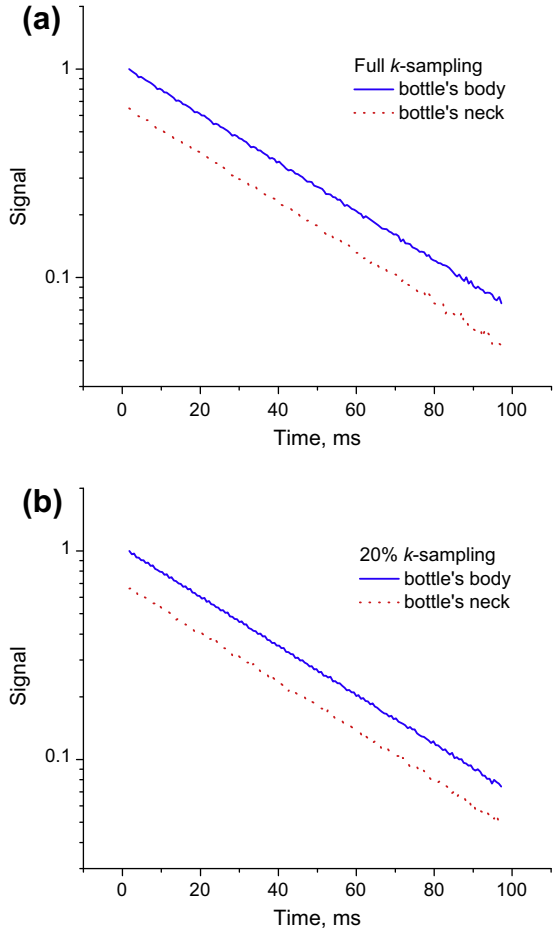

Fig. 7. Pixel-resolved T_2 decays obtained from SE-SPI experiments with full (a) and 20% k-sampling (b).

appears to be less robust compared to the CPMG-prepared SPRITE. What is important, however, is that spatially resolved T_2 measurements seem to be insensitive to these factors (see Fig. 7). In this case, providing an image that is simply free of aliasing (wrap-around artifacts) seems to be sufficient for T_2 mapping. Owing to the limited first echo acquisition time in 2-D SE-SPI, resulting T_2 distributions miss components shorter than 2 ms. For the same reason, it gives disproportionate image intensities for components with different diffusivity (e.g. water and oil), as opposed to CPMG-SPRITE (compare Figs. 4 and 9).

To conclude, 2-D SE-SPI and CPMG-SPRITE demonstrate a similar performance, enabling measurement of T_2 down to 1–2 ms. Both experiments are time consuming (up to 2–2.5 h in our examples). As such, they can be recommended only for measurement during steady state conditions or when studying relatively slow dynamic processes.

5. Experimental

NMR measurements were carried out on an Oxford Instruments DRX spectrometer equipped with a 0.35 T horizontal bore General Electric (GE) magnet ($\nu = 15$ MHz), at room temperature. GE gradient coils provided a maximum gradient strength of 170 mT/m. The r.f. probe was a home-made 54-mm diameter birdcage probe, with a 90°-pulse duration of 19 μs at 50% attenuation. T_2 distributions were measured by using the UPEN Laplace inverse transform algorithm [11].

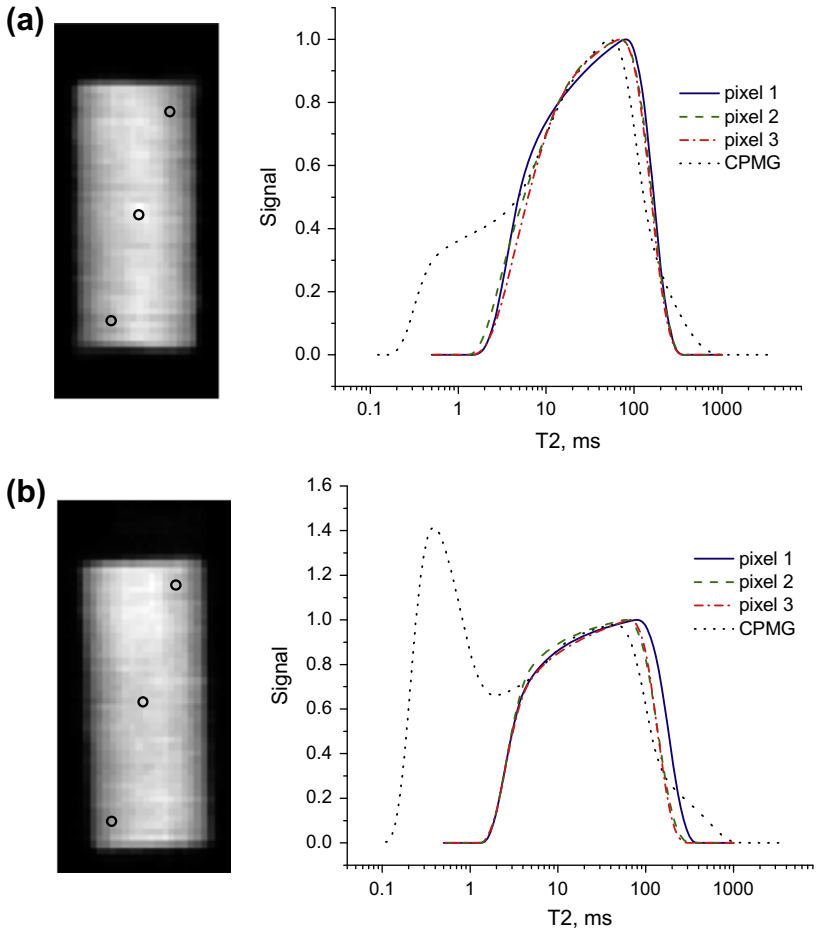

Fig. 8. (a, left) A 64 × 32 SE-SPI image of Berea sandstone saturated with water. (a, right) T_2 distributions measured at three different pixels across the sample, in comparison to the measurements by regular CPMG. (b) As above but for Wallace sandstone.

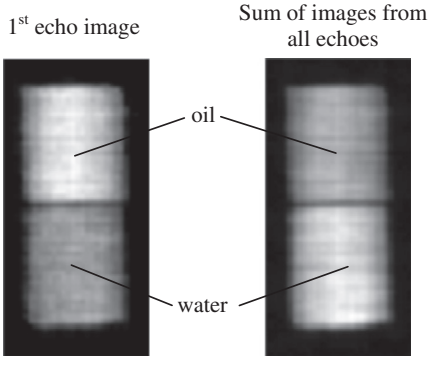

Fig. 9. 64 × 32 SE-SPI images of oil- and water-saturated pieces of Wallace sandstone. Unlike in Fig. 4, the 1st echo image shows considerably different intensities for oil and water, which is attributed to the diffusion attenuation of the water signal during τ_0 (see Fig. 5a).

Acknowledgments

This research was supported by NSERC of Canada, Petroleum Research Atlantic Canada, the Canada Chairs Program, and Conoco Phillips. We thank Thomas Goldstein, the University of California, for helpful discussion regarding the Split Bregman algorithm for compressed sensing.

Appendix A

Consider an arbitrary element of a pulse sequence with a low flip angle α and a period TR. The evolution of the z-magnetization within this element between $t = 0^+$ and $t = TR$ can be written as

$$M_z(TR) = M_{eq} - \Delta M_{eq}(0^+)e^{-TR/T_1},$$

where $\Delta M_{eq} = M_{eq} - |M_z(0^-)|\cos\alpha$ is a deviation from magnetization in the thermodynamic equilibrium, M_{eq}, and $t = 0^-$ and $t = 0^+$ denote the moments immediately before and after an α-pulse. If the prepared magnetization $M_{z,1}(0^-)$ points to $+z$, then we have after the first α-pulse:

$$M_{z,1}(TR) = M_{z,1}(0^-)\cos\alpha e^{-TR/T_1} + M_{eq}(1 - e^{-TR/T_1}),$$

after the second pulse:

$$M_{z,2}(TR) = M_{z,1}(0^-)\left(\cos\alpha e^{-TR/T_1}\right)^2 + M_{eq}\left(1 - e^{-TR/T_1}\right) + M_{eq}\left(1 - e^{-TR/T_1}\right)\cos\alpha e^{-TR/T_1},$$

and after the n-th pulse:

$$M_{z,n}(TR) = M_{z,1}(0^-)\left(\cos\alpha e^{-TR/T_1}\right)^n + M_{eq}\left(1 - e^{-TR/T_1}\right)\frac{1 - \left(\cos\alpha e^{-TR/T_1}\right)^n}{1 - \cos\alpha e^{-TR/T_1}}, \quad (A.1)$$

When the prepared magnetization $M_{z,1}(0^-)$ points to $-z$, it becomes

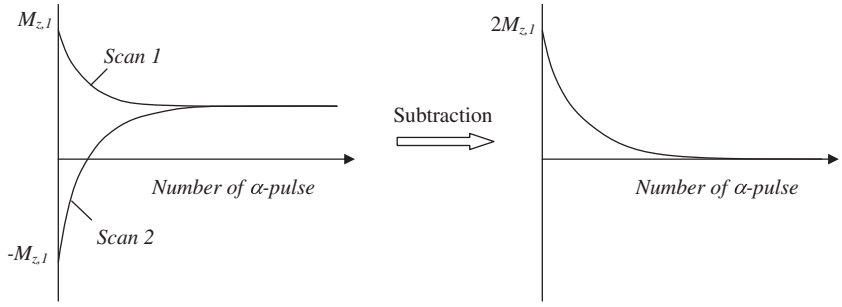

Fig. A1. Illustration of the idea of the two-scan acquisition with alternating z-storage (after [2]).

$$M_{z,n}(TR) = -M_{z,1}(0^-)\left(\cos\alpha\, e^{-TR/T_1}\right)^n + M_{eq}\left(1 - e^{-TR/T_1}\right)\frac{1-\left(\cos\alpha\, e^{-TR/T_1}\right)^n}{1-\cos\alpha\, e^{-TR/T_1}} \quad (A.2)$$

Subtracting (A.2) from (A.1) gives

$$\tilde{M}_{z,n}(TR) = 2M_{z,1}(0^-)\left(\cos\alpha\, e^{-TR/T_1}\right)^n, \quad (A.3)$$

thus canceling the 'unprepared' magnetization contribution (the second term in (A.1) and (A.2)). This is illustrated graphically in Fig. A1.

Appendix B

Here, we outline the image reconstruction procedure used in SE-SPI. Let x denote the image of interest and y the acquired undersampled k-space signal. For irregular k-samples on a rectangular grid (''compressed sensing data''),

$$y = F_u x + e, \quad (B.1)$$

where e is measurement noise and F_u is the undersampled FFT operator (2-D FFT followed by omitting respective Fourier modes). The ordinary least-squares solution of (B.1) is unstable and considered impracticable. Instead, one estimates x seeking the minimum of an objective function

$$\min_x \|\Psi x\|_1 + \frac{\mu}{2}\|F_u x - y\|_2^2, \quad (B.2)$$

where (B.1) is used as a quadratic error term, and the first term (l_1-regularizer) diminishes variability of the solution. The operator ψ represents one of the sparsifying transforms, which include total variation transform, wavelet transform, discrete cosine transform or principle components decomposition.

To minimize (B.2), we use the Split Bregman algorithm for compressed sensing [7]. Introducing a new variable $d = \Psi x$, (B.2) is rewritten in the ''split Bregman'' formulation

$$\min_{x,d} \|d\|_1 + \frac{\mu}{2}\|F_u x - y\|_2^2 + \frac{\lambda}{2}\|d - \Psi x - b\|_2^2 \quad (B.3)$$

with the Bregman feedback parameter b included in the second least-square term. It is then minimized iteratively with respect to x and d, updating b at the end of an iteration:

$$x^{k+1} = \arg\min_x \frac{\mu}{2}\|F_u x - y\|_2^2 + \frac{\lambda}{2}\|d^k - \Psi x - b^k\|_2^2 \quad (B.4)$$

$$d^{k+1} = \arg\min_d \|d\|_1 + \frac{\lambda}{2}\|d - \Psi x^{k+1} - b^k\|_2^2 \quad (B.5)$$

$$b^{k+1} = b^k + \Psi x^{k+1} - d^{k+1} \quad (B.6)$$

Thus, the original, hard to solve, problem (B.2) is decomposed into two sub-problems (B.4) and (B.5) for x and d, which are relatively easy. The sub-problem (B.4) is differentiable and can be solved via two FFT's [7], and the optimization in (B.5) is performed through simple soft shrinkage procedures (for motivation for shrinkage see, e.g., [12]). Once the optimal values of x and d are found within a given tolerance (inner loop), the Bregman update is applied to y (outer loop).

We use the Matlab code of this algorithm by T. Goldstein, available from www.math.ucla.edu/≃tagoldst/code.html, ported to the IDL programming language with minor additions (namely, the second, Haar wavelet, l_1-regularizer has been added, according to [7]). The number of the inner loops was 40 and the outer loops 8, which took about 1.5 s per a 64 × 32 image on a Pentium 4 PC laptop.

References

[1] O.V. Petrov, G. Ersland, B.J. Balcom, T_2 distribution mapping profiles with phase encode MRI, Journal of Magnetic Resonance 209 (2011) 39–46.
[2] A.A. Khrapitchev, B. Newling, B.J. Balcom, Centric-scan SPRITE magnetic resonance imaging with prepared magnetisation, Journal of Magnetic Resonance 181 (2006) 271–279.
[3] M. Halse, J. Rioux, S. Romanzetti, J. Kaffanke, B. MacMillan, I. Mastikhin, N.J. Shah, E. Aubanel, B.J. Balcom, Centric scan SPRITE magnetic resonance imaging: optimization of SNR, resolution, and relaxation time mapping, Journal of Magnetic Resonance 169 (2004) 102–117.
[4] T. Gullion, D.B. Baker, M.S. Conradi, New, compensated Carr–Purcell sequences, Journal of Magnetic Resonance 89 (1990) 479–484.
[5] P.D. Majors, J.L. Blackley, S.A. Altobelli, A. Caprihan, E. Fukushima, Eddy-current compensation by direct field detection and digital gradient modification, Journal of Magnetic Resonance 87 (1990) 548–553.
[6] E.J. Candes, M.B. Wakin, An introduction to compressive sampling, IEEE Signal Processing Magazine 25 (2008) 21–30.
[7] T. Goldstein, S. Osher, The split Bregman method for l1-regularized problems, SIAM Journal on Imaging Sciences 2 (2009) 323–343.
[8] J. Dahl, P.C. Hansen, S.H. Jensen, T.L. Jensen, Algorithms and software for total variation image reconstruction via first-order methods, Numerical Algorithms 53 (2010) 67–92.
[9] P. Parasoglou, A.J. Sederman, J. Rasburn, H. Powell, M.L. Johns, Optimal k-space sampling for single point imaging of transient systems, Journal of Magnetic Resonance 194 (2008) 99–107.
[10] P. Parasoglou, D. Malioutov, A.J. Sederman, J. Rasburn, H. Powell, L.F. Gladden, A. Blake, M.L. Johns, Quantitative single point imaging with compressed sensing, Journal of Magnetic Resonance 201 (2009) 72–80.
[11] G.C. Borgia, R.J.S. Brown, P. Fantazzini, Uniform-penalty inversion of multiexponential decay data, Journal of Magnetic Resonance 132 (1998) 65–77.
[12] A. Chambolle, R.A. DeVore, N.Y. Lee, B.J. Lucier, Nonlinear wavelet image processing: variational problems, compression, and noise removal through wavelet shrinkage, IEEE Transactions on Image Processing 7 (1998) 319–335.
[13] M.H. Levitt, Composite pulses, Progress in Nuclear Magnetic Resonance Spectroscopy 18 (1986) 61–122.